MRS Communications (2024) 14:1000–1006

https://doi.org/10.1557/s43579-024-00630-8

MRS Communications

Early Career Materials Researcher Research Letter

Determining the oxidation stability of SnSe under atmospheric exposure

Jonathan R. Chin, Bonnie G. Gardner, and Marshall B. Frye, School of Materials Science and Engineering, Georgia Institute of Technology, Atlanta, GA, USA
Derrick S-H. Liu, Department of Materials Science and Engineering, The Pennsylvania State University, University Park, PA, USA; 2D Crystal Consortium Materials Innovation Platform, The Pennsylvania State University, University Park, PA, USA
Sebastian A. Marini, Department of Materials Science and Engineering, Cornell University, Ithaca, NY, USA
Jeffrey Shallenberger, Materials Research Institute, The Pennsylvania State University, University Park, PA, USA
Matthew T. McDowell, School of Materials Science and Engineering, Georgia Institute of Technology, Atlanta, GA, USA; George W. Woodruff School of Mechanical Engineering, Georgia Institute of Technology, Atlanta, GA, USA
Maria Hilse, Department of Materials Science and Engineering, The Pennsylvania State University, University Park, PA, USA; 2D Crystal Consortium Materials Innovation Platform, The Pennsylvania State University, University Park, PA, USA; Materials Research Institute, The Pennsylvania State University, University Park, PA, USA
Stephanie Law, Department of Materials Science and Engineering, The Pennsylvania State University, University Park, PA, USA; 2D Crystal Consortium Materials Innovation Platform, The Pennsylvania State University, University Park, PA, USA; Materials Research Institute, The Pennsylvania State University, University Park, PA, USA; Penn State Institute of Energy and the Environment, The Pennsylvania State University, University Park, PA, USA
Lauren M. Garten, School of Materials Science and Engineering, Georgia Institute of Technology, Atlanta, GA, USA

Address all correspondence to Lauren M. Garten at **Lauren.garten@mse.gatech.edu**

(Received 2 April 2024; accepted 19 August 2024; published online: 19 September 2024)

Abstract

Understanding surface stability becomes critical as 2D materials like SnSe are developed for piezoelectric and optical applications. SnSe thin films deposited by molecular beam epitaxy showed no structural changes after a two-year exposure to atmosphere, as confirmed by X-ray diffraction and Raman spectroscopy. X-ray photoelectron spectroscopy and reflectivity show a stable 3.5 nm surface oxide layer, indicating a self-arresting oxidative process. Resistivity measurements show an electrical response dominated by SnSe post-exposure. This work shows that SnSe films can be used in ambient conditions with minimal risk of long-term degradation, which is critical for the development of piezoelectric or photovoltaic devices.

Introduction

Tin selenide (SnSe) has significant potential for piezoelectric and non-linear optoelectronic applications but only when scaled down to a single layer to induce a non-centrosymmetric crystal structure.[1–3] However, a monolayer of SnSe could become more susceptible to surface effects from defects and oxidation. Oxidative corrosion in other 2D materials such as graphene, black phosphorus, and transition-metal dichalcogenides (TMDs) has been shown to have an adverse effect on multiple mechanical and electrical properties, including corrosion resistance and conductivity.[4–6] Given the ease with which oxidation occurs in 2D TMDs,[7,8] there is a risk that the oxygen present in the air could impact the stability of monolayer SnSe, limiting its potential applications in practical settings. Yet few studies have investigated the effect of atmospheric exposure on the bulk and surface chemical stability of post-transition-metal monochalcogenides.

First-principles calculations of the oxidative degradation of monolayer group-IV monochalcogenides indicate that GeS, GeSe, SnS, and SnSe should have high activation energies for the chemisorption of O_2, decreasing the likelihood of oxidation.[9] However, previous reports have shown the formation of SnO_2 layers in SnSe bulk crystals that were exposed to oxygen at temperatures greater than 100°C.[10] Similarly, SnO_2 has been found to remain stable up to 600°C in thermoelectric studies.[11,12] SnO_2 has also been observed on SnSe thin films synthesized between 65 and 95°C using an adsorption/diffusion method in air, but the extent and impact of these oxide layers were not investigated.[13] Overall, the extent of oxidation throughout SnSe thin films at room temperature and its impact on the electrical response has not yet been established. It is also not clear how surface or bulk reactions in SnSe progress over time when exposed. Understanding how the surface and bulk of SnSe thin films change when exposed to atmosphere is important for not only engineering SnSe devices, but also for integrating monochalcogenides with other materials. Thus, reaching the full potential of SnSe applications requires understanding both the surface interactions and the extent of oxidation throughout the SnSe thin film.

This work investigates the sensitivity of the surface and bulk of SnSe thin films to atmospheric exposure. The composition and structure of SnSe thin films are assessed immediately after growth, at six months, and after a two-year period of atmospheric exposure. Tracking the structure and composition over an extended period of exposure time provides further insight into the limited progression of oxidative degradation in the films over time. X-ray diffraction (XRD), Raman spectroscopy, X-ray reflectivity (XRR), and X-ray photoelectron spectroscopy (XPS) taken upon initial exposure and after extended times in atmosphere show the limited extent of oxidative

degradation in SnSe. Overall, this work provides critical insight into the stability and surface reactions in SnSe thin films.

Materials and methods

Tin selenide (SnSe) thin films were grown via molecular beam epitaxy (MBE) onto (100) magnesium oxide (MgO) substrates (MTI Corp). MgO ($a = 4.29$ Å) was selected as the substrate because it has a close lattice match with the *b*–*c* plane of *Pnma* SnSe ($a = 11.490$ Å, $b = 4.440$ Å, $c = 4.135$ Å).[16,29] Prior to growth, the MgO substrates were annealed at 1000 ℃ for 80 min in a tube furnace with an oxygen gas flow of 80 sccm, after which they were cleaned via ultrasonication in acetone, then isopropyl alcohol, and finally deionized water for 5 min each before transfer into the MBE chamber. To establish the conditions for stoichiometric growth, the Sn and Se fluxes were each measured with a quartz crystal monitor prior to growth. SnSe depositions were conducted in an ultra-high vacuum (UHV) environment with a base pressure of 9.0×10^{-10} Torr for 80 min at 275 ± 5℃ with a Se:Sn flux ratio of 1.5 ± 0.2 to 1 and a growth rate of 0.3 Å/s.

The next step was to determine the impact of atmospheric exposure on the surface and bulk stability of the MBE-grown SnSe films. SnSe thin films that were grown under the same conditions were either exposed to atmosphere immediately following growth or kept in a vacuum enclosure to be exposed after 6 months or 2 years. The data from the samples exposed for 2 years will be used except where specified. The impact of exposure was assessed by X-ray photoelectron spectroscopy (XPS), X-ray diffraction (XRD), and Raman Spectroscopy. The chemical composition of the films was measured using a Physical Electronics VersaProbe II and a Thermo K-Alpha X-ray photoelectron spectrometer, both with Al Kα sources (1486.6 eV) and a flood gun to reduce charging effects. Charge offset corrections were made by adjusting the adventitious carbon C1s peak to 284.8 eV.[30] XPS peak fittings were performed using the Powell algorithm with a Gauss-Lorentz convolution in the *Avantage* software. A SnSe single crystal that was not exposed to atmosphere was used as a calibration standard for XPS, from which we derived the empirical sensitivity factors for a 1:1 Sn:Se stoichiometry. To derive the sensitivity factors, an Ar ion etch was performed on the SnSe bulk crystal to measure the Sn:Se ratio. Because the stoichiometry of the single crystal is 1:1, a new sensitivity ratio is defined such that this ratio is maintained. This correction factor is subsequently applied to the thin-film depth profiles. The Ar ion etch rate of SnSe was determined by comparing the etch time when the Sn and Se XPS peaks disappeared to the film thicknesses determined by transmission electron microscopy.[14]

The crystallographic phase and orientation of each film were characterized after exposure using a high-resolution Panalytical X'Pert^3 4-circle X-ray diffraction (XRD) system as well as a Panalytical Empyrean XRD, both with a PIXcel 3D detector and Cu $K_{\alpha 1}$ source. The observed differences in K(Lα), K(Lβ) and tungsten peaks result from the two different XRD systems. X-ray reflectivity (XRR) measurements were conducted on a Rigaku Smartlab XE with a Cu $K_{\alpha 1}$ source. The reliability factor (R-factor) in the XRR fitting serves as an indication of the discrepancy between the raw data and the applied model, with a lower R-factor being a better fit. A Horiba LabRam Raman spectrometer with a 532 nm laser and a Renishaw inVia Qontor Raman spectrometer with a 488 nm laser were also used to characterize the thin-film crystal structure. For the scanning transmission electron microscopy (STEM), a layer of AuPd was sputter coated onto the top of the SnSe samples using a Quorum Q150V ES Plus to help image the ceramic sample for the Thermo Fisher Helios 5CX focused ion beam scanning electron microscope (FIB-SEM). FIB-SEM was necessary to isolate a cross section of the sample. The FIB lamella was plasma cleaned for one minute under oxygen plasma. STEM data were acquired on the ThermoFisher Spectra300 aberration corrected STEM, operating at 200 kV accelerating voltage. High-angle annular dark field (HAADF) image was acquired with a 30 mrad convergence angle, 80 mrad collection angle, nominal screen current on the scale of 100 pA, and pixel time of 32 us. Corresponding electron energy loss spectra (EELS) line scan was acquired under the same conditions, except the exposure for each spectrum was 0.5 s. These conditions were chosen to minimize electron beam damage.

Electrical measurements were conducted using a Squidstat Plus Potentiostat/Galvanostat along with a Signatone S-302 four-point resistivity probe with 1 mm probe tip spacing. All electrical measurements were conducted in the dark to minimize photocurrent contributions. Galvanostatic Electrical Impedance Spectroscopy tests were run on a 150 nm thick sample of SnSe. The AC current frequency was varied from 1 MHz to 1 Hz with 20 steps recorded per decade, 5 s of quiet time, and an amplitude of 20 nA. Electrical impedance spectroscopy (EIS) data were fitted using AfterMath impedance fitting software and an equivalent circuit consisting of 3 parallel RC units in series. Due to the low current amplitude, high-frequency data had significant amounts of noise. All data shown in the Nyquist plot were used for the equivalent circuit fit except for any points with a negative real or imaginary impedance value as well as two points of clear noise at 63 and 56 Hz were removed from consideration. The resistivity of the thin films after exposure was determined by plotting an I/V curve on the same four-point system. Current was varied from 0—30 nA in 5 nA intervals, and the resulting voltage was measured by the Squidstat system. Plotting I vs V and fitting these data with a linear line of best fit enabled the resistance to be found using the slope of the fitted line. Taking into account several correction factors necessary due to the size, shape, and thickness of the sample, the resistivity was able to be calculated using the relationship $\rho = 2\pi s F \frac{V}{I}$, where s is the probe tip spacing, F is the product of the necessary correction factors,

and $\frac{V}{I}$ is the slope of the IV curve. F_{11}, the correction factor for a thin sample with a non-conducting bottom wafer surface, can be calculated following $F_{11} = \frac{t/s}{2In\,(2)}$ where t is the layer thickness, and s is the probe spacing distance when t is less than half of s. F_2, the correction factor for the lateral dimensions of a sample, can be calculated according to $F_2 = \frac{In\,(2)}{In\,(2)+In\left[\left(\frac{D}{S}\right)^2+3\Big/\left(\frac{D}{S}\right)^2-3\right]}$ where D is the sample width for rectangular samples. F_3 is the correction factor for probe placement when probes are a non-infinite distance from the edges of the sample. However, this correction factor only varies appreciably from unity when the distance from the edge exceeds 2 mm, and all measurements done on this sample had a distance from any edge of at least 2 mm.[25]

Results and discussion

Figure 1(a) shows 2θ X-ray diffraction (XRD) scans taken on an 85-nm-thick chalcogenide thin film immediately upon atmospheric exposure and on the same films after two years of exposure. The XRD data fit to the *Pnma* phase of SnSe with a predominant {200} out-of-plane orientation demonstrated by the intense diffraction peaks observed up to the fourth order ($n=4$).[14] All other starred peaks are associated with Kβ or tungsten lines from the substrate. There is no difference in the XRD peak positions before or after the prolonged atmospheric exposure, indicating that significant bulk degradation of the SnSe films did not occur when exposed to air. No other secondary phases are observed. Specifically, there is no evidence of crystalline SnO_2 by XRD (the expected XRD peaks characteristic of SnO_2 would be at 26°, 34°, 52°, 55°, 58°, and 62°) after exposure, despite the propensity of Sn to oxidize.[12] These results suggest that if any crystalline oxide layer or secondary phase is present, it must be limited to concentrations below the detection limit of the XRD. Given that it can be difficult to observe films below 5 nms by standard XRD, grazing-incidence X-ray diffraction (GIXRD) was employed which enables the detection of the (211) plane of SnO_2 at 52°, as shown in Fig. S1. Additionally, there is no change in the out-of-plane layer spacing upon exposure; the same peaks belonging to the {200} plane family of SnSe peaks are present in both cases, and the d-spacing is consistent. These results indicate that there is not significant intercalation of oxygen or other molecules between the layers of the 2D structure. The consistent layer spacing suggests that any oxidation is limited to the surface and does not progress through the material or between the layers.

Further evidence for the stability of SnSe after the prolonged atmospheric exposure comes from the Raman spectra in Fig. 1(b). The vibrational modes at 70 cm^{-1}, 108 cm^{-1}, 130 cm^{-1}, and 150 cm^{-1} correspond to the A_g^2, A_g^3, B_{3g}, and A_g^4 vibrational modes attributed to SnSe, respectively.[15,16] An extended Raman spectrum is included in Fig. S2 to demonstrate that there are no clear indications of modes associated with SnO_2, which would be expected at 330 cm^{-1}, 620 cm^{-1}, or 760 cm^{-1}. No other phases are observed by Raman spectroscopy. The offset in vertical spacing has been intentionally introduced to make clear the equivalent peak positions in each spectrum.

Slight differences in Raman shift could be attributed to the different wavelengths and filters used in the separate Raman spectrometers between the one-hour and two-year measurements. Given that the Raman peaks have the same width and relative peak intensities before and after two years of exposure, this indicates that no significant changes to the bulk of the material have occurred because of the atmospheric exposure. Additionally, as with XRD, there are no obvious signs of SnO_2 formation or other secondary phases.

While the XRD and Raman results show that the film's structure is unaffected by prolonged exposure to air, subtle changes in surface or layer chemistry could still occur that can impact the electrical performance. Thus, it is critical to assess any changes in the elemental composition at the surface and between the layers of the SnSe thin films after the

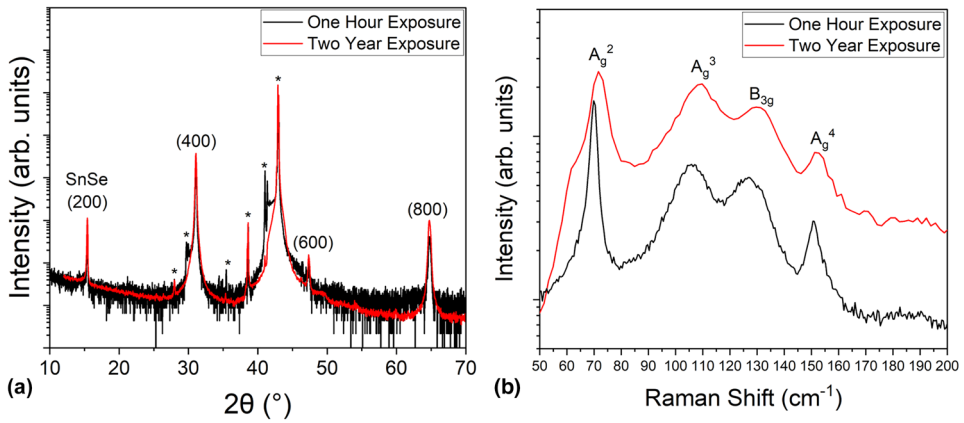

Figure 1. (a) XRD of a SnSe thin film grown on MgO immediately upon atmospheric exposure and after a period of two years. The (*h*00) peak labels in the XRD are attributed to SnSe, and peaks labeled with * are from the substrate, Kβ, and tungsten lines, and (b) the Raman spectra of the same SnSe thin film after a one-hour exposure and a film grown with the same conditions after a period of 2 years. All Raman peaks are fit to SnSe.

extended atmospheric exposure. Figure 2(a) features depth profiles taken from X-ray photoelectron spectroscopy (XPS) tracking the relative atomic percents for each element present in SnSe thin films on MgO. This depth profile was taken immediately after the growth, with 20 s etch increments. During the etch Ar ions ablate Se at a faster rate than Sn, which leads to an inaccurate selenium count in the compositional measurement. To compensate for this, empirical sensitivity factors are derived from an equivalent ion etch of a pristine SnSe bulk single crystal, shown in Fig. S3. Once calibrated using the sensitivity factor, Sn and Se appear in near-equal amounts throughout the sample indicating stoichiometric SnSe. A significant O 1 s peak is observed prior to etching, indicating that there is an oxide layer at the surface of the film. The etch depth at each step is approximately 7 nm; thus, a precise thickness of the oxide layer cannot be determined below this threshold by XPS alone.

Figure 2(b) shows a comparative XPS depth profile for the same SnSe thin film (etched in a different location on the same sample) after prolonged exposure to atmosphere. The relative amounts of Sn and Se present are approximately equal, as was the case before the exposure. Similarly, just as with the initial XPS measurements, oxygen is exclusively at the surface of the SnSe thin films, indicating that the oxide layer has not increased in thickness or progressively degraded the film. Again, the depth profiles indicate that the oxide layer on the surface of the sample is self-limiting. The difference in time to etch down to the substrate is due to the use of two different XPS instruments. While the ion beam parameters were made as similar as possible, each instrument has an individual etch rate that differs per material.

Analyzing the Sn and Se peaks from the surface of the etched SnSe thin film provides further insight into the surface composition. The asymmetrical Sn XPS peaks at 485.6 and 486.7 eV in Fig. 2(c), taken from the surface of the sample prior to depth profiling, are attributed to SnSe and SnO_2, respectively.[10] In the literature, there is some variation in the Sn 3d binding energies, ranging from 485.6 eV[17] to 486.6 eV[13] for SnSe and 486.7 eV[17] to 487.2 eV[18] for the SnO_2, but in all cases, the Sn 3d peak in SnO has a higher binding energy.[18] In this work to further corroborate the SnSe binding energy, scans are taken on a pristine SnSe single crystal, shown in Fig. S3. The results for the single crystal provide a standard to identify the location of the binding energies for tin and selenium when the oxide is absent, which is determined to be 486.3 eV and 53.6 eV, respectively. Thus, the peak at 486.7 is attributed to SnO_2.

It is not surprising that the surface of SnSe has an oxide layer, as the formation of tin oxide on Sn metal and Sn alloys is well documented,[19,20] with the most stable oxides for tin being SnO, SnO_2, and Sn_3O_4.[21] The fact that peaks corresponding to both SnO_2 and SnSe are visible in the surface scan suggests

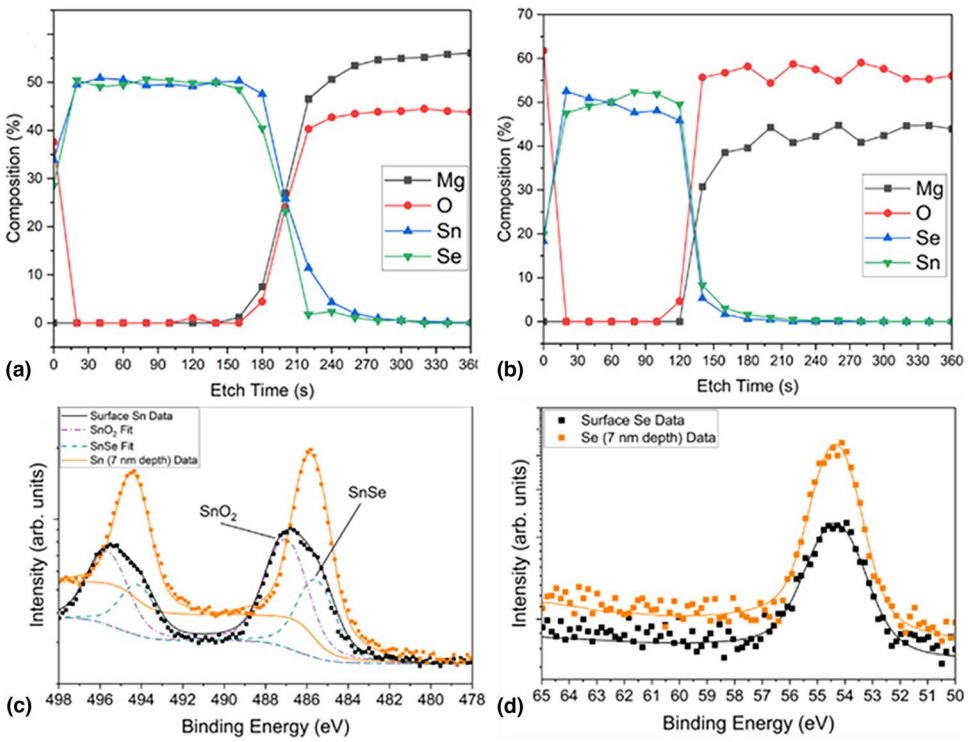

Figure 2. XPS measurements of a single 85-nm-thick SnSe thin-film sample grown on MgO showing (a) a XPS depth profile immediately after exposure to atmosphere; (b) a XPS depth profile after two years of atmospheric exposure; (c) the Sn 3d scan at the surface and after a 20 s etch to a depth of approximately 7 nm on the SnSe sample exposed for two years; and (d) the binding energy of Se 3d at the surface and one etch level of 20 s, also to a depth of approximately 7 nm on the SnSe sample exposed for 2 years.

that the SnO_2 layer is less than 5 nm, the average measurement depth of an XPS system. As the etch continues into the films the stoichiometry becomes solely SnSe with no oxide peaks present, speaking to the chemical stability of the layered structure within the SnSe thin film. Similar analysis on the XPS characterization of oxidation states in SnSe thin films has shown that peaks corresponding to SnO_2 disappear upon surface etching, suggesting that the oxide is limited to the surface.[13] It should also be noted that the Sn binding energy for SnO is 486.6 eV, which is indistinguishable from SnO_2 at 486.7 eV, particularly this close to the SnSe peak.[13] However, the case of SnO_2 on SnSe thin films is more well documented. The Se post-etch scans on the SnSe thin film in Fig. 2(d) shows that the Se 3d peak at and beneath the surface has a binding energy of 54.5 eV, corresponding to the Sn–Se bond in SnSe.[22]

X-ray reflectivity (XRR) measurements provide further insight on the thickness, quality, and density of the surface oxide layer and the SnSe film after exposure. The data shown in Fig. 3 are for a SnSe film exposed to atmosphere for a period of 6 months. The XRR scan is fitted with a model that includes the MgO substrate, a 34.7-nm-thick layer of SnSe, and a 3.6 nm layer of SnO_2,[23] yielding an R-factor of 0.518%. The model parameters are given in greater detail in Table S1. The fitted SnSe density is 5.24 g/cm^3, which is 8.9% less than the expected 5.75 g/cm^3 density, which could stem from the stepped terraced grain structure of the SnSe film. If SnO_2 is excluded from the model, then the R-factor is 3.046%. This relationship holds for the 2 year exposure as well, shown in Fig. S4. The model of SnSe with SnO_2 has a much lower R-factor than the model of SnSe alone, indicating that an ultrathin, surface layer of tin oxide is present. The fitted density of the SnO_2 is 3.95 g/cm^3, which is much less than the expected 6.95 g/cm^3, indicating that there is not complete surface coverage or variable thickness of SnO_2. Partial surface area oxidation is expected because 2D chalcogenide thin films are known to resist oxidation except in locations where there are defects in the surface such as vacancies or dangling bonds.[24] Additionally, the limited thickness of the surface oxide layer can be inferred from the surface XPS data in Fig. 3(c), where the Sn–Se bonds can still be detected at the surface. The XRR in combination with the XRD and XPS indicate that oxidation is limited to the exposed surface and does not progress through the material. Similarly, Fig. S5 includes a transmission electron microscope (TEM) measurement of a cross section of 10-nm-thick SnSe on MgO exposed for two years. These TEM/EELS results show a discrete layer that is approximately 3.5 nm layer thick above the SnSe thin film. The thickness measurements are shown in Fig. S5(b). It should be noted that the deposition of this metal layer for FIB could have caused damage to the film, which might explain why the surface layer looks more amorphous by TEM than would be expected from the GIXRD results (Fig. S1). The corresponding electron energy loss spectroscopy (EELS) shows no oxygen counts within the bulk SnSe layer, further demonstrating the self-arresting nature of any surface-localized Sn oxide.

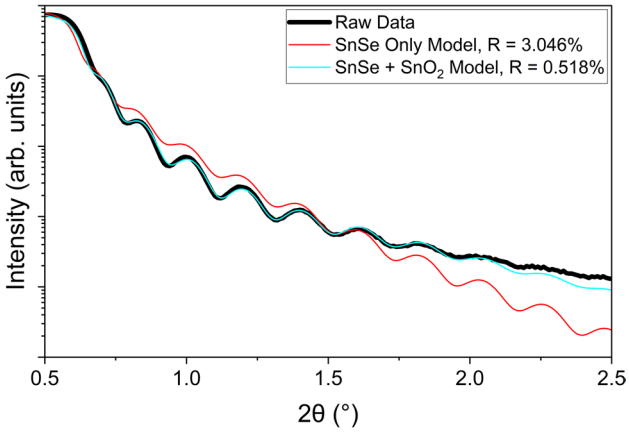

Figure 3. XRR of a SnSe thin film grown on MgO and exposed to atmosphere for 6 months with fits for SnSe alone and SnSe with SnO_2.

To evaluate the impact of the surface oxide on the electrical response of SnSe films, the resistivity is assessed via current–voltage (IV) measurements taken via four-point galvanostatic metrology on a SnSe thin film grown under the same conditions as the films in Fig. 2. The IV plot is shown in Fig. S6. The resistivity extracted from the IV data is approximately 14.4 Ωcm.[25] These results indicate that the electrical response is dominated by SnSe as the total resistivity is closer to the electrical resistivity of SnSe (1.2×10^{-2} Ωcm) than that of SnO_2 (5.49×10^6 Ωcm).[26,27] However, the oxide is found to impact the EIS measurements of the SnSe film. The Nyquist plot in Fig. 4 covers a frequency range from 1 Hz to 1 MHz. The best fit to this data is a 3-component equivalent circuit due to the multiple local maxima, the high feature asymmetry, and the suppression of Z". The equivalent circuit, shown inset in Fig. 4, uses a 3 resistor–capacitor circuit and yields a χ^2 value of 0.917. These results indicate a complex electrical response stemming from not only the bulk material but also the interfaces between the chalcogenide and oxide layer and between the oxide layer and the probe.[28] The lower-frequency contributions could also indicate internal conduction of charge or ions between SnSe layers under applied electric fields, but further analysis is needed to determine the dominant physical mechanism behind this response. Overall bulk resistance extracted from the x-axis intersection of the curve on the Nyquist plot of 200 kW agrees with the value experimentally obtained from the slope of the IV plot, further confirming that the electrical response from this material is predominantly due to the SnSe.

The combination of methods used here indicates that the bulk crystal structure and composition of SnSe are stable under atmospheric exposure. The oxide layer that forms is ultrathin and stable. The formation of the oxide layer occurs on shorter time scales than what was tested here, as the layer was seen in samples measured immediately after exposure. While an oxide layer does form on the film surface, the results show that there is not an increase in the amount of oxide with continued

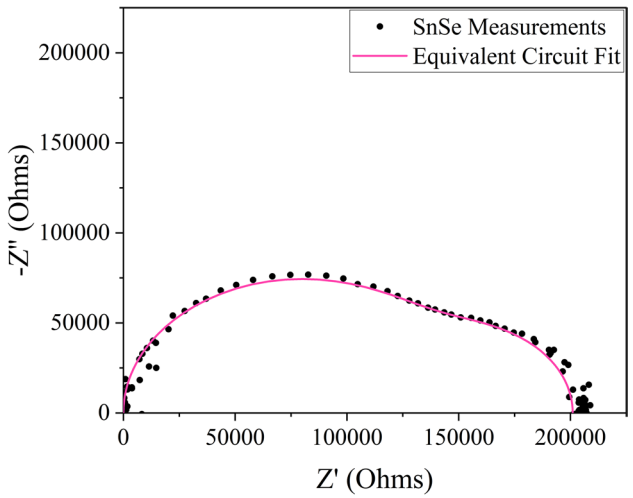

Figure 4. Nyquist plot of the electrical impedance spectroscopy (EIS) measurements taken after 2 years of atmospheric exposure. The inset shows the equivalent circuit used for fitting.

exposure to air over a period of 2 years, indicating that the process of oxidation is self-limiting. Given that the oxide layer is more insulating than the bulk material and does not impact the materials composition or structure past a few nanometers, this oxide provides a useful passivation layer for electronic and optoelectronic applications. This means that SnSe thin films can be incorporated into devices that operate in ambient conditions with minimal risk of short- or long-term degradation resulting from air exposure. An insulating surface layer is particularly useful for piezoelectric devices based on SnSe given that the unique polar axis is in the plane of the film, and thus, lateral device fabrication is necessary. With an insulating surface layer, it is assured that the piezoelectric response will not be short circuited by a conductive surface layer. Additionally, adding indium dopants to the surface could lead to the formation of an indium-doped tin oxide, ITO, which is a transparent top contact often used in photovoltaics. The benefits of the passivating oxide layer are expected to persist as the layer thickness of SnSe is scaled down to the single-layer limit. However, further work is necessary to verify the thickness of the oxide layer below the nm scale limit of XRR measurements established in this work. Finally, the benefits and formation of this oxide layer are likely similar in materials isostructural to SnSe, like the other layered post-transitional metal monochalcogenides GeSe, and SnS.

Conclusions

Understanding the long-term chemical stability and self-limiting surface oxidation of SnSe is critical for the development of electronic and optoelectronic devices. Exposing SnSe thin films to atmosphere for two years did not induce changes in the bulk chemical composition or crystal structure of the films. An oxide layer formed on the film surface after exposure, but XPS depth profiles and XRR show that the SnO_2 is localized to 3.6 nm or less from the surface of the SnSe thin films. IV measurements yield a resistivity value closer to that of SnSe rather than that of the more resistive SnO_2, suggesting that the bulk of the material's electrical response is dictated by SnSe, but the EIS response indicates that the interface created with the oxide layer does play a role in the electrical response. Overall, the exposure to atmosphere did not lead to significant structural or chemical changes and the surface layer was found to be self-limiting. The oxide layer that forms on SnSe is passivating and will not consume the material over the expected lifetime of a practical device.

Acknowledgments

LMG acknowledges the Air Force Office of Scientific Research (AFOSR) Young Investigator Award under Grant No. FA9550-22-1-0237. JRC acknowledges the support of the National Science Foundation (NSF) Graduate Research Fellowship Program under Grant No. DGE-2039655. BG, MM, and LMG acknowledge the support of the Office of Naval Research, Navy Undersea Research Program (NURP) through contract N00014-23-1-2367. The work presented has been facilitated by the Materials Innovation Platform of The Pennsylvania State University, the Two-Dimensional Crystal Consortium (2DCC-MIP), supported by NSF through cooperative agreements no. DMR-1539916 and DMR-2039351. This work was performed in part at the Georgia Tech Institute for Electronics and Nanotechnology, a member of the National Nanotechnology Coordinated Infrastructure (NNCI), which is supported by the National Science Foundation (Grant ECCS-2025462). STEM work was performed at the University of Tennessee—Knoxville, Electron Microscopy Center.

Author contributions

Materials synthesis was conducted by Jonathan Chin, Marshall Frye, Lauren Garten, Derrick Liu, and Maria Hilse. XRD and Raman were conducted by Jonathan Chin, Marshall Frye, Derrick Liu, and Maria Hilse. XPS was conducted by Jeffrey Shallenberger, Bonnie Gardner, Sebastian Marini, and Matthew McDowell. Electrical measurements were conducted by Bonnie Gardner and Mathew McDowell. The study was designed by Lauren Garten, Maria Hilse and Stephanie Law. The efforts were led by Stephanie Law, Matthew McDowell, Maria Hilse, and Lauren Garten. The paper draft was written by Jonathan Chin. All authors contributed to the manuscript and approved of the final submission.

Funding

Air Force Office of Scientific Research, FA9550-22-1-0237, Lauren M. Garten, National Science Foundation Graduate Research Fellowship Program, DGE-2039655, Jonathan Robert Chin, Office of Naval Research Global,N00014-23-1-2367,

Lauren M. Garten, National Science Foundation, DMR-1539916, DMR-2039351, ECCS-2025462, Office of Science

Data availability

The data comprising the results of this paper are included in the following link for transparency: https://m4-2dcc.vmhost.psu.edu/list/data/xBzRVQNFDZ92.

Declarations

Conflict of interest

On behalf of all authors, the corresponding author states that there is no conflict of interest.

Supplementary Information

The online version contains supplementary material available at https://doi.org/10.1557/s43579-024-00630-8.

Open Access

References

1. I. Ronneberger, Z. Zanolli, M. Wuttig, R. Mazzarello, Adv. Mater. **32**, e2001033 (2020). https://doi.org/10.1002/adma.202001033
2. Q. Zhu, K. Zhang, D. Li, N. Li, J. Xu, D.W. Bahnemann, C. Wang, Chem. Eng. J. **426**, 131681 (2021). https://doi.org/10.1016/j.cej.2021.131681
3. M. Kumar, S. Rani, Y. Singh, K.S. Gour, V.N. Singh, RSC Adv. **11**, 6477–6503 (2021). https://doi.org/10.1039/d0ra09807h
4. J. Yang, X. Liu, Q. Dong, Y. Shen, Y. Pan, Z. Wang, K. Tang, X. Dai, R. Wu, Y. Jin, W. Zhou, S. Liu, J. Sun, Chin. Chem. Lett. **33**, 177–185 (2022). https://doi.org/10.1016/j.cclet.2021.06.078
5. A. Iqbal, J. Hong, T.Y. Ko, C.M. Koo, Nano Converg. **8**, 9 (2021). https://doi.org/10.1186/s40580-021-00259-6
6. Q. Li, Q. Zhou, L. Shi, Q. Chen, J. Wang, J. Mater. Chem. A Mater. Energy Sustain. **7**, 4291–4312 (2019). https://doi.org/10.1039/c8ta10306b
7. S. Tanwar, A. Arya, A. Gaur, A.L. Sharma, J. Phys. Condens. Matter **33**, 303002 (2021). https://doi.org/10.1088/1361-648X/abfb3c
8. G. Gong, M. Li, N. Sun, T. Zhi, Y. He, J. Pan, Y. Cai, L. Wang, Chin. Chem. Lett. (2023) 108705. https://doi.org/10.1016/j.cclet.2023.108705.
9. Y. Guo, S. Zhou, Y. Bai, J. Zhao, A.C.S. Appl, Mater. Interfaces **9**(2017), 12013–12021 (2020). https://doi.org/10.1021/acsami.6b16786
10. S. Badrinarayanan, A.B. Mandale, V.G. Gunjikar, A.P.B. Sinha, J. Mater. Sci. **21**, 3333–3338 (1986). https://doi.org/10.1007/bf00553376
11. S. Shimizu, K. Miwa, T. Kobayashi, Y. Tazawa, S. Ono, Sci. Rep. **11**, 1637 (2021). https://doi.org/10.1038/s41598-021-81195-7
12. Y. Li, B. He, J.P. Heremans, J.-C. Zhao, J. Alloys Compd. **669**, 224–231 (2016). https://doi.org/10.1016/j.jallcom.2016.01.258
13. R. Ivanauskas, A. Kunciute, I. Ancutiene, M. Andrulevicius, M. Mikolajunas, Surf. Interfaces **28**, 101675 (2022). https://doi.org/10.1016/j.surfin.2021.101675
14. J.R. Chin, M.B. Frye, D.S.-H. Liu, M. Hilse, I.C. Graham, J. Shallenberger, K. Wang, R. Engel-Herbert, M. Wang, Y.K. Shin, N. Nayir, A.C.T. van Duin, L.M. Garten, Nanoscale **15**, 9973–9984 (2023). https://doi.org/10.1039/d3nr00645j
15. X. Xu, Q. Song, H. Wang, P. Li, K. Zhang, Y. Wang, K. Yuan, Z. Yang, Y. Ye, L. Dai, A.C.S. Appl, Mater. Interfaces **9**, 12601–12607 (2017). https://doi.org/10.1021/acsami.7b00782
16. T. Sriv, T.M.H. Nguyen, Y. Lee, S.Y. Lim, V.Q. Nguyen, K. Kim, S. Cho, H. Cheong, Sci. Rep. **10**, 11761 (2020). https://doi.org/10.1038/s41598-020-68744-2
17. M.R. Burton, T. Liu, J. McGettrick, S. Mehraban, J. Baker, A. Pockett, T. Watson, O. Fenwick, M.J. Carnie, Adv. Mater. **30**, e1801357 (2018). https://doi.org/10.1002/adma.201801357
18. M. Fondell, M. Gorgoi, M. Boman, A. Lindblad, J. Electron Spectrosc. Relat. Phenom. **195**, 195–199 (2014). https://doi.org/10.1016/j.elspec.2014.07.012
19. W.E. Boggs, J. Electrochem. Soc. **108**, 124 (1961). https://doi.org/10.1149/1.2428026
20. S.B. Lyon, Elsevier, 2010: pp. 2068–2077. https://doi.org/10.1016/b978-044452787-5.00099-8.
21. J. Leitner, D. Sedmidubský, J. Phase Equilibria Diffus. **40**, 10–20 (2019). https://doi.org/10.1007/s11669-018-0686-4
22. M.N. Ashiq, S. Irshad, M.F. Ehsan, S. Rehman, S. Farooq, M. Najam-Ul-Haq, A. Zia, New J. Chem. **41**, 14689–14695 (2017). https://doi.org/10.1039/c7nj04030j
23. T. Yamanaka, R. Kurashima, J. Mimaki, Zeitschrift Für Kristallograph. Crystal. Mater. **215**, 424–428 (2000). https://doi.org/10.1524/zkri.2000.215.7.424
24. Y. Guo, S. Zhou, J. Zhao, ChemNanoMat **6**, 838–849 (2020). https://doi.org/10.1002/cnma.201900492
25. D.K. Schroder, John Wiley & Sons, Inc, 2006: pp. 1–59. https://catalogimages.wiley.com/images/db/pdf/9780471739067.excerpt.pdf.
26. N.E. Makori, I.A. Amatalo, P.M. Karimi, W.K. Njoroge, Am. J. Condens. Matter Phys. **4**, 87–90 (2014). https://doi.org/10.5923/j.ajcmp.20140405.01
27. F. Yakuphanoglu, Electrical conductivity. J. Alloys Compd. **470**, 55–59 (2009). https://doi.org/10.1016/j.jallcom.2008.03.013
28. Y. Zhang, L. Li, S. Yuan, G. Li, W. Zhang, Electrochim. Acta **109**, 221–225 (2013). https://doi.org/10.1016/j.electacta.2013.07.152
29. S. Kaneko, T. Tokumasu, Y. Nakamaru, C. Kokubun, K. Konda, M. Yasui, M. Kurouchi, M. Can, S. Shawuti, R. Sudo, T. Endo, S. Yasuhara, A. Matsuda, M. Yoshimoto, Jpn. J. Appl. Phys. **58**, SAAD06 (2019). https://doi.org/10.7567/1347-4065/aaec11
30. D.K. Aswal, K.P. Muthe, S. Tawde, S. Chodhury, N. Bagkar, A. Singh, S.K. Gupta, J.V. Yakhmi, J. Cryst. Growth **236**, 661–666 (2002). https://doi.org/10.1016/S0022-0248(02)00852-7